Patched Zero-Velocity-Bouncing Trajectories: A Low-Energy Path Planning Strategy

Kenta Oshima

Hiroshima Institute of Technology
Hiroshima, Japan
Email:k.oshima.nt@cc.it-hiroshima.ac.jp

***Abstract* – This paper develops a graph-aided framework for efficiently computing low-energy transfer trajectories in a multi-objective fashion. A challenging exploration of the high-dimensional phase space is relaxed by introducing special apsis conditions, with which pivotal dynamical objects in the low-energy regime such as zero-velocity surfaces and periodic orbits associate. Flight time and delta-v characteristics for transitioning between periapsis-to-periapsis arcs represent weighted directed graphs. A variety of solutions in challenging examples is generated as a shortest path in the graph that is robustly optimized by a regularized fuel minimizer.**

I. INTRODUCTION

Low-energy transfers leveraging the multi-body gravitational environment are often useful for reducing fuel costs, but their computations are not straightforward due to the non-negligible third-body perturbation. The absence of general solutions leads to the use of special solutions or a brute force approach.

The former typically leverages dynamical objects such as periodic/quasi-periodic orbits and stable/unstable manifolds embedded in a region targeted by a specific mission. Since they are coasting arcs, optimal chaining would naturally produce fuel-efficient solutions. The selection of appropriate dynamical objects may be possible in a well-studied problem, but it should be nontrivial in general and depend on each region of interest and user's experience. In other words, such an approach may lack versatility. Another difficulty of handling dynamical objects in the high-dimensional phase space in spatial or non-autonomous models also exists.

The latter approach may be free from the aforementioned defects, but a clear disadvantage is the computational burden. Even in a simplified autonomous model such as the circular restricted three-body problem (CR3BP) adopting a surface of section, 5-dimensional phase space should at least be explored. A comprehensive search with a fine enough resolution would be computationally demanding.

Despite the challenging task of exploring the high-dimensional search space, the recent trend of piggyback CubeSats requires the rapid trajectory design as the launch condition can be subject to last minute changes [1]. In this regard, one of our aims is to develop an efficient method of computing a variety of low-energy transfer trajectories.

A graph-aided approach may be one means of realizing efficient trajectory design as a graph can store the information of discretized states as well as their connectivity. Tsirogiannis (2012) [2] proposed the use of a graph consisting of discretized states of periodic orbits and associated chaining impulses. Dijkstra's algorithm [3] was used to find an optimal path in the graph. Parrish (2014) [4] applied A* algorithm [5] that is a heuristic extension of Dijkstra's algorithm to compute low-thrust trajectories. Das-Stuart et al. (2020) [6] used Dijkstra's algorithm to compute low-thrust trajectories in the CR3BP. These earlier works struggled with the large graph size sharply affected by the resolution of discretization. Trumbauer and Villac (2014) [7] discretized states at periapsis and expanded the efficiency of the graph-aided approach. Still, they were suffered from the aforementioned 5-dimensional search and a global trade-off analysis was not carried out. Bellome et al. (2023) [8] performed a multi-objective analysis by combining the Lambert-based graph transcription and the dynamic programming technique in the patched two-body model. Although not implementing pathfinding algorithms, Hiraiwa et al. (2023) [9] used a graph structure consisting of regions enclosed by stable and unstable manifolds to simplify the selection of transfer paths.

The present paper develops a graph-aided framework for efficiently computing low-energy transfer trajectories in a multi-objective fashion within the spatial CR3BP. We assume the use of the method for designing reference trajectories in such a way that general-purpose large graphs are precomputed and stored and once a mission analysis begins, specific boundary conditions are translated and added to the graphs so that a pathfinding algorithm is applied and candidate solutions are optimized. Besides the efficiency due to the separable feature of the general precomputing and specific mission analysis phases, our method is versatile in the sense that it is applicable to various regions in a unified manner regardless of the existence of distinct objects governing phase-space transport such as libration point orbits and resonant orbits and associated stable/unstable manifolds.

In the remainder of the paper, Section II introduces the

mathematical model. Section III describes each component of the computational process. Section IV presents application examples.

II. Mathematical Model

This study uses the spatial CR3BP to prove the concept of the proposed approach. The model describes the motion of a massless particle under the gravitational influence of two celestial bodies of masses m_1 and m_2 $(m_1 \geq m_2)$ that move in circular orbits around their barycentre. In our case, a particle is a spacecraft and gravitational bodies are Earth and the Moon. Non-dimensional equations of motion in a rotating reference frame are [10]

$$\dot{x} = v_x, \dot{y} = v_y, \dot{z} = v_z, \quad \dot{v}_x = 2v_y - \frac{\partial \bar{U}}{\partial x}, \dot{v}_y = -2v_x - \frac{\partial \bar{U}}{\partial y}, \dot{v}_z = -\frac{\partial \bar{U}}{\partial z}, \tag{1}$$

where

$$\bar{U} = -\frac{1}{2}(x^2 + y^2) - \frac{1-\mu}{r_1} - \frac{\mu}{r_2} - \frac{1}{2}\mu(1-\mu), \tag{2}$$

$$r_1 = \sqrt{(x+\mu)^2 + y^2 + z^2}, \tag{3}$$

$$r_2 = \sqrt{(x-1+\mu)^2 + y^2 + z^2}, \tag{4}$$

$$\mu = m_2/(m_1 + m_2).$$

The conservative nature of the system admits the existence of a constant of motion called Jacobi energy:

$$C = -\left({v_x}^2 + {v_y}^2 + {v_z}^2\right) - 2\bar{U}. \tag{5}$$

The CR3BP is an autonomous system and the dimensionality of the phase space is six. Handling higher-fidelity time-dependent models with another dimensionality is beyond the scope of the present paper.

III. Design Framework

Our framework consists of a general precomputing phase that is independent of a specific mission requiring heavier computational resources and a mission analysis phase applying specific constraints. Since they are separable, most of the effort of exploring the high-dimensional phase space can be completed before a specific mission analysis begins. Fig. 1 illustrates computational processes in the framework.

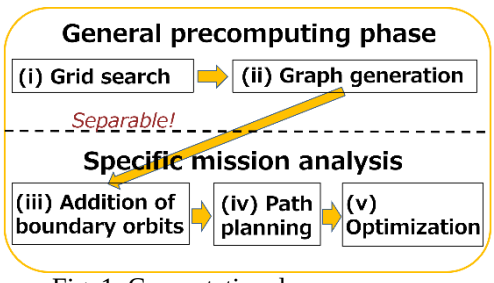

Fig. 1. Computational processes.

A. Grid Search

The present work firstly computes trajectories from periapsis to periapsis. An apsis (periapsis or apoapsis) condition can be expressed as

$$\dot{r}_i = 0 \ (i = 1 \text{ or } 2), \tag{6}$$

which indicates that the dimensionality of the search space is five. However, a comprehensive search in the 5-dimensional space is computationally demanding. Even though it is admissible, memory or storage issues would arise as the resultant graph size sharply grows with the increase of the output of the grid search.

To relax the dimensionality of the search space, the present paper introduces special apsis conditions. Note that (6) can be rewritten as

$$(x - x_i^*)v_x + yv_y + zv_z = 0 \ (i = 1 \text{ or } 2), \tag{7}$$

where x_i^* denotes the abscissa of the gravitational body in the rotating reference frame.

Therefore, the following eight special conditions, which are termed special apsis conditions, satisfy the general apsis condition (6):

$$v_x = v_y = v_z = 0 \tag{8}$$
$$v_x = v_y = z = 0 \tag{9}$$
$$v_x = y = v_z = 0 \tag{10}$$
$$v_x = y = z = 0 \tag{11}$$
$$x - x_i^* = v_y = v_z = 0 \tag{12}$$
$$x - x_i^* = v_y = z = 0 \tag{13}$$
$$x - x_i^* = y = v_z = 0 \tag{14}$$
$$x - x_i^* = y = z = 0 \tag{15}$$

Each of these special conditions constrains three variables and thus the dimensionality of the search space becomes three. In summary, instead of exploring the 5-dimensional search space associated with (6), we explore the 3-dimensional search space for each of the special conditions (8)-(14). The present paper excludes (15) as it corresponds to a singular point. Note that (8) yields zero-velocity surfaces whereas (10) and (11) include states on symmetric periodic orbits indicating the possibility of leveraging these pivotal dynamical objects in the low-energy regime.

To compute periapsis-to-periapsis arcs, initial conditions satisfying each of (8)-(14) are distributed on grids in the corresponding 3-dimensional search space. If $\ddot{r}_i < 0$ (apoapsis), the initial condition is propagated forward and backward in time until reaching periapsis. If $\ddot{r}_i > 0$ (periapsis), the initial condition is propagated forward and backward in time until reaching apoapsis, then further propagated until reaching periapsis. In both cases, state transition matrices (STMs) associated with apoapsis-to-periapsis interval as well as states on apsides and flight time between apsides are stored.

B. Graph Generation

In this paper, each of the periapsis-to-periapsis arcs expresses a graph node whereas defining the connectivity between nodes, i.e., edges, requires further

information. It is not economical in terms of storage and memory to connect all pairs of nodes as many of them would be fuel-inefficient transfers. To exclude impractical connections and define edge weights, we use the fixed-time-of-arrival (FTA) method [11] to calculate chaining Δv. The analytical mapping by the STMs enables the calculation for all pairs of the periapsis-to-periapsis arcs.

Fig. 2 illustrates the FTA method of calculating impulses ($\Delta \boldsymbol{v}_a$ at apoapsis and $\Delta \boldsymbol{v}_p$ at periapsis) for connecting a pair of periapsis-to-periapsis arcs at the periapsis of the succeeding arc. Using the STM $\Phi^{A,P}$ associated with the apoapsis-to-periapsis interval of the preceding arc, the impulses can be calculated as

$$\Delta \boldsymbol{v}_A = \Phi_{rv}^{A,P\,-1}\left(\boldsymbol{r}_p^+ - \boldsymbol{r}_p^-\right), \tag{16}$$

$$\Delta \boldsymbol{v}_P = \boldsymbol{v}_p^+ - \boldsymbol{v}_p^- - \Phi_{vv}^{A,P}\Delta \boldsymbol{v}_A, \tag{17}$$

where

$$\Phi^{A,P} = \begin{bmatrix} \Phi_{rr}^{A,P} & \Phi_{rv}^{A,P} \\ \Phi_{vr}^{A,P} & \Phi_{vv}^{A,P} \end{bmatrix}$$

and $\{\boldsymbol{r}_p^+, \boldsymbol{v}_p^+\}$ and $\{\boldsymbol{r}_p^-, \boldsymbol{v}_p^-\}$ indicate periapsis position and velocity vectors of succeeding and preceding arcs, respectively, and $\{\boldsymbol{r}_a^-, \boldsymbol{v}_a^-\}$ represent apoapsis position and velocity vectors of a preceding arc before applying $\Delta \boldsymbol{v}_a$. Note that $\Delta \boldsymbol{v}_a$ cancels the position error whereas $\Delta \boldsymbol{v}_p$ cancels the velocity error at the patch point. As the name of the method indicates, the flight time $\Delta t = t_p^1 - t_p^0$ is invariant under the application of $\Delta \boldsymbol{v}_A$.

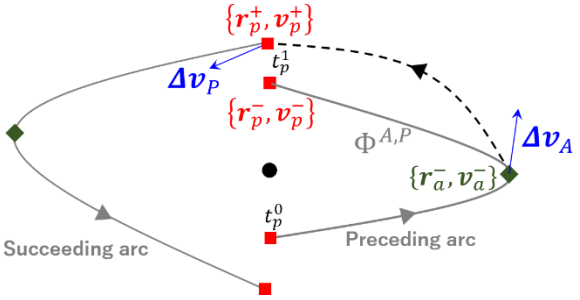

Fig. 2. FTA method. The solid line represents periapsis-to-periapsis arcs and the dashed line indicates a corrected arc. The dot, square, and diamond denote the central body, periapsis, and apoapsis, respectively.

These two impulses are used to exclude fuel-inefficient connections. However, the small difference in velocity directions at periapsis can lead to the large magnitude of $\Delta \boldsymbol{v}_P$ that may be drastically reduced in numerical optimization via further adjustments. Therefore, we normalize the magnitude of $\Delta \boldsymbol{v}_P$ and only approve graph edges satisfying both of the following conditions:

$$|\Delta \boldsymbol{v}_a| < \Delta v_a^{max}, \tag{18}$$

$$|\Delta \boldsymbol{v}_p| / |\boldsymbol{v}_p^+| < \Delta v_p^{max}. \tag{19}$$

Positive weights are assigned to the approved edges so that a multi-objective analysis in terms of flight time and fuel cost can be carried out. We define

$$w = \alpha \Delta t + \beta(1-\alpha)\Delta v, \tag{20}$$

where

$$\Delta v = \gamma |\Delta \boldsymbol{v}_a| + \delta(1-\gamma)\Delta v_p^{min} \tag{21}$$

and β and δ are tuning constants so that α and γ are linearly varied in the interval $[0\ 1]$. Here, Δv_p^{min} is a theoretical minimum Δv_p [12] that estimates the magnitude of $\Delta \boldsymbol{v}_P$ as a tangential impulse as

$$\Delta v_p^{min} = \left| \sqrt{-2\bar{U}(\boldsymbol{r}_p^+) - C(\boldsymbol{r}_p^+, \boldsymbol{v}_p^+)} - \sqrt{-2\bar{U}(\boldsymbol{r}_p^+) - C(\boldsymbol{r}_a^-, \boldsymbol{v}_a^- + \Delta \boldsymbol{v}_a)} \right|. \tag{22}$$

Note that (22) only extracts a role of varying Jacobi energy. In summary, (20) aims to explore the trade-off between flight time and Δv by varying α whereas (21) considers the balance between $\Delta \boldsymbol{v}_a$ and $\Delta \boldsymbol{v}_p$ playing complementary roles by varying γ.

Since switching preceding and succeeding arcs results in different edge connectivity and weights, our graph is a weighted directed graph. We generate and store a graph for each of $11 \times 11 = 121$ combinations of α and γ.

To generate a graph, the information of source and target nodes corresponding to approved pairs of preceding and succeeding arcs, respectively, and their edge weights is required. One favourite way is to construct and pass an adjacency matrix $A(s,t)$ whose entry (s,t) represents a weight of an edge connecting source and target nodes of indices s and t $(s,t \in \mathrm{N})$. This intuitive expression however needs to store zeros for unapproved edge weights before converting into a graph that is inefficient in terms of memory. The present paper instead adopts an edge list consisting of three vectors representing indices of only approved source and target nodes and their edge weights.

C. Addition of Boundary Arcs and Pathfinding

Once a specific mission analysis begins, mission boundary arcs and associated connections shall be translated into graph nodes and edges that are added to the precomputed general-purpose graphs explained in the previous section. To be consistent with the FTA analysis, a periapsis-to-periapsis arc is extracted from the final part of the initial mission orbit and a periapsis state to be connected is determined as an initial point of the final mission orbit. New indices of the graph nodes are provided to the initial and final arcs. Note that an initial state of the initial orbit and a final state of the final orbit are not necessarily periapsides.

Using the FTA method, chaining impulses are calculated by regarding the periapsis-to-periapsis arc of the initial orbit as a preceding arc and the other arcs except for the final orbit as succeeding arcs in Fig. 2. Moreover, those connecting with the final orbit are calculated by treating periapsis-to-periapsis arcs including that of the initial orbit as preceding arcs and the final orbit as a succeeding arc.

In a similar manner to the previous section, pairs of preceding and succeeding arcs satisfying both (18) and (19) are only approved and their edge weights are calculated. Newly determined indices of source and target nodes and corresponding edge weights are added to the precomputed graphs for each combination of α and γ.

An initial guess solution is identified as a path in each of the graphs resulting in the minimum sum of the weights. Since the weights are always positive according to (20), Dijkstra's algorithm [3] is applied to solve this shortest path problem. Despite the difference in α and γ, some solutions can be identical and thus redundant ones are removed from a solution set to be optimized.

D. Local Optimization

Resultant initial guess solutions are multi-impulse multi-revolutional trajectories that may encounter highly nonlinear events including flybys and stable/unstable manifold-based transport. To robustly optimize such trajectories, the present paper applies two transformations to regularize the problem and enhance the robustness of convergence into fuel-optimal solutions.

Fig. 3 illustrates the multiple shooting procedure adopted in the present study. The subscripts regulate the order of shooting nodes and the superscripts indicate states before (minus) or after (plus) applying impulses. The states $\boldsymbol{X}_j^+$ correspond to $\{\boldsymbol{r}_p^+, \boldsymbol{v}_p^+\}$ and $\{\boldsymbol{r}_a^-, \boldsymbol{v}_a^- + \Delta\boldsymbol{v}_A\}$ in Fig. 2. Each segment is further divided into five segments to enhance the robustness.

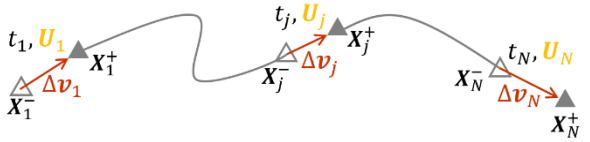

Fig. 3. Multiple shooting method.

Following Oshima (2024) [13], a vector of regularized variables $\boldsymbol{U}_j = [u_j\ w_j\ s_j]^{\mathrm{T}}$ expresses a Δv vector based on the Kustaanheimo-Stiefel transformation [14] as

$$\Delta\boldsymbol{v}_j = \begin{bmatrix} {u_j}^2 - {w_j}^2 - {s_j}^2 \\ 2u_j w_j \\ 2u_j s_j \end{bmatrix} \tag{23}$$

yielding

$$\left|\Delta\boldsymbol{v}_j\right| = \left|\boldsymbol{U}_j\right|^2 \tag{24}$$

and

$$\partial\left|\Delta\boldsymbol{v}_j\right| / \partial\boldsymbol{U}_j = 2{\boldsymbol{U}_j}^{\mathrm{T}}. \tag{25}$$

This transformation removes the singularities associated with zero-magnitude impulses from derivatives of an objective function $J = \sum_{j=1}^{N}\left|\Delta\boldsymbol{v}_j\right|$. See [13] for details of implementation.

The present study also considers the regularization with respect to time. As mentioned earlier, each segment between apsides is further divided by shooting nodes, which may be initially distributed with an equal interval in time as illustrated in Fig. 4 (left). Shooting nodes localize around the region where the motion is slow that may cause bias in terms of the resolution of states and controls. This is particularly true when building an initial guess solution patched on zero-velocity surfaces based on (8).

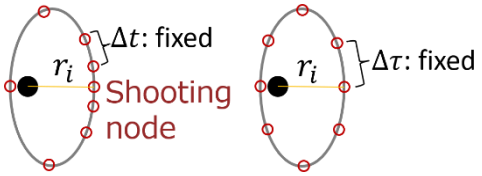

Fig. 4. Distribution of shooting nodes.

Following Yam et al. (2010) [15], the present paper applies the Sundman transformation [16] and introduces fictitious time τ as

$$dt = r_i\, d\tau \quad (i = 1 \text{ or } 2). \tag{26}$$

Equation (26) transforms the original equations of motion in (1) compactly expressed as

$$d\boldsymbol{X}/dt = \boldsymbol{F}(\boldsymbol{X})$$

into

$$d\boldsymbol{X}/d\tau = r_i\, \boldsymbol{F}(\boldsymbol{X}), \qquad dt/d\tau = r_i \tag{27}$$

changing the independent variable from t to τ.

Shooting nodes are initially distributed with an equal interval in fictitious time between apsides as illustrated in Fig. 4 (right). Equation (27) is numerically integrated to compute trajectories. This procedure relaxes the localization of shooting nodes at the cost of increasing the number of variables.

IV. Applications:

This section presents two examples of applying the developed framework for computing a variety of low-energy transfer trajectories in the Earth-Moon CR3BP. The following simulations use a pure MATLAB environment on Windows 11 workstation with Intel(R) Xeon(R) Gold 6240 CPU, 64.0 GB RAM, and 2.60 GHz clock speed.

A. Halo-to-Halo Transfer

The first example is a transfer problem between southern halo orbits with periods of 7.5 [days] and 13.6 [days] associated with the L_2 libration point. Since this is a well-studied problem in earlier works [17-20], it would be ideal to understand the potential of the present method by comparing the solutions.

Table 1 summarizes grid search conditions in the 3-dimensional search space. The superscripts A and P indicate the search conditions applied to apoapsis and

periapsis, respectively. Note that the other three variables are determined from (8)-(14).

Table 1. Grid search conditions in the first example

Variable	Minimum	Maximum	Number of grids
x	0.75	1.25	100
y	-0.25	0.25	
z	-0.25	0.25	
v_x^A	-0.75	0.75	
v_y^A	-0.75	0.75	
v_z^A	-0.75	0.75	
v_x^P	-2.5	2.5	
v_y^P	-2.5	2.5	
v_z^P	-2.5	2.5	

The initial conditions are further screened and those satisfying the following conditions are selected for the subsequent propagation:

$$R_m < r_2 < 2r_{Hill}, \qquad C_{L3} < C < 3.3, \qquad (28)$$

where R_m is the Moon's radius, r_{Hill} is the Hill radius of the Moon, and C_{L3} is Jacobi energy at the L_3 libration point.

During the computation of periapsis-to-periapsis arcs, those violating the former condition in (28) are excluded. The FTA method is applied to the obtained arcs with $\Delta v_a^{max} = 30$ [m/s] and $\Delta v_p^{max} = 0.5$ to disapprove fuel-inefficient connections. 121 Graphs are generated and stored from the arcs and approved connections with $\beta = 50$ and $\delta = 1$.

Fig. 5 shows specific initial and final arcs. Since the initial halo orbit is weakly unstable, the initial state of an unstable manifold, which is a perturbed state at apolune with the magnitude of 10^{-4}, is further perturbed [21] to the unstable direction with $\Delta v = 5$ [m/s]. The left and centre panels correspond to different signs of perturbation. The final arc (right panel) is a usual stable manifold emanating from an apolune state with the perturbation magnitude of 10^{-4}.

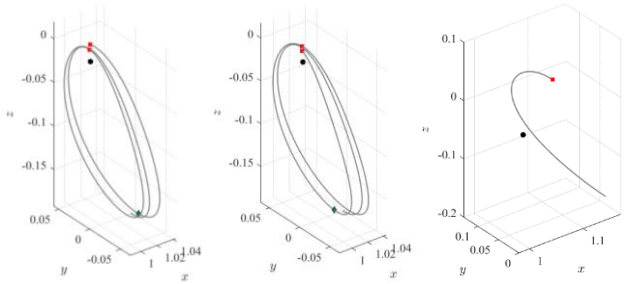

Fig. 5. Initial (left and central) and final (right) arcs in the first example. The dot, square, and diamond denote the Moon, periapsis, and apoapsis, respectively.

Graph nodes corresponding to the initial and final arcs and edges representing their connectivity are added to the precomputed graphs, to which Dijkstra's algorithm is applied to find initial guess solutions. Among 29 unique solutions, those of the total transfer time shorter than 100 [days] are optimized. In the optimization process, perilune states are constrained to be higher than 1000 [km] from the lunar surface [20].

Fig. 6 compares the obtained solutions with those found in the earlier works. The theoretical minimum value is calculated from Jacobi energy of the halo orbits and the perilune state of the initial halo orbit that is regarded as a departure point.

Our method successfully finds a Pareto-like frontier in the interval of 45-85 [days]. The minimum-Δv solution almost reaches the theoretical minimum indicating the end of a frontier. On the other hand, our method could not explore the solution space whose transfer time is shorter than 40 [days]. This comes from the application of the tolerances in (18) and (19) excluding fuel-inefficient edges. Larger tolerances increase the ability of finding solutions of shorter transfer time at the cost of larger graph size. Fig. 6 clearly highlights suitable targets in our method are low-Δv solutions that are usually sought when designing low-energy trajectories.

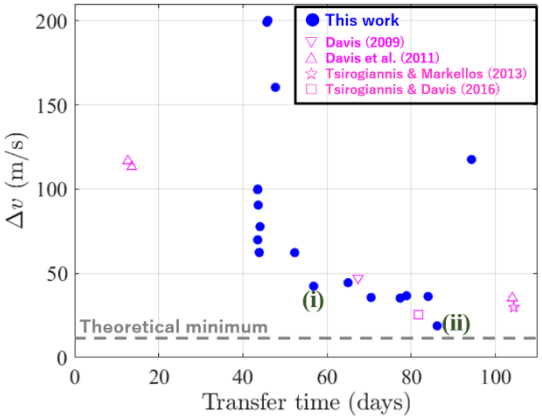

Fig. 6. Comparison of solutions.

Figs. 7 and 9 show initial guess trajectories of (i) and (ii) indicated in Fig. 6, respectively, and Figs. 8 and 10 exhibit the corresponding optimized solutions including time histories of impulses and Jacobi energy. The orbital characteristics are qualitatively preserved by optimization.

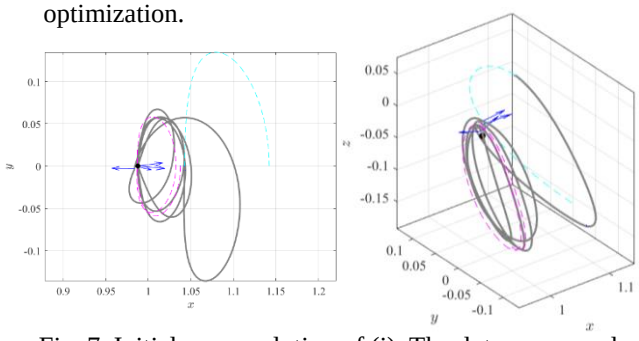

Fig. 7. Initial guess solution of (i). The dot, arrow, and dashed curve denote the Moon, impulse, and stable/unstable manifold, respectively.

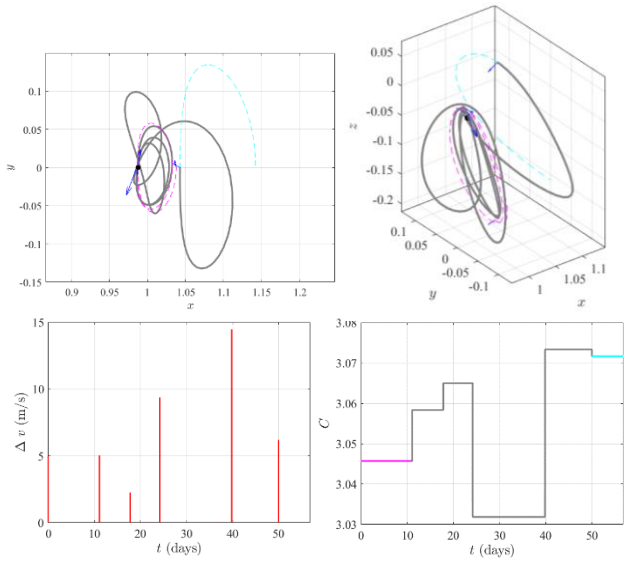

Fig. 8. Optimal solution (i). The dot, arrow, and dashed curve denote the Moon, impulse, and stable/unstable manifold, respectively.

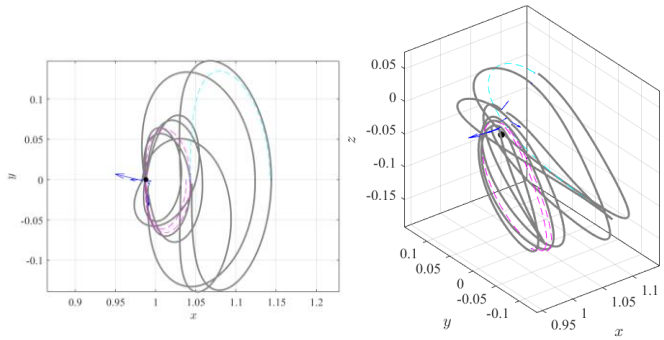

Fig. 9. Initial guess solution of (ii). The dot, arrow, and dashed curve denote the Moon, impulse, and stable/unstable manifold, respectively.

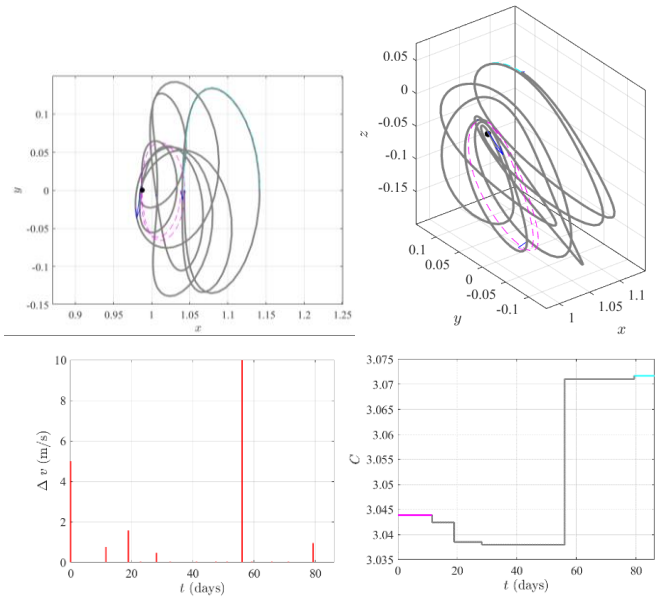

Fig. 10. Optimal solution (ii). The dot, arrow, and dashed curve denote the Moon, impulse, and stable/unstable manifold, respectively.

Table 2 summarizes the computational performance in this example. Note that the general precomputing phase composed of the grid search and graph generation processes accounts for the majority of the running time that can be separately carried out from the specific mission-related analysis.

A drawback of the present framework is the riesig size of the output files in the second process consisting of 121 large graphs that must be stored for arbitrary mission analyses. A forthcoming work may handle this issue. The large memory allocation in the third process required for accessing the large graphs in parallel causes the small available number of CPU cores. The number of CPU cores used in the optimization process simply corresponds to the number of initial guess solutions.

Table 2. Computational performance in the first example

Process	Running time	Core	Output
Grid search	26 [min]	36	0.77 [GB]
Graph generation	11.5 [hour]	36	144 [GB]
Addition of boundary arcs and pathfinding	37 [min]	3	4 [kB]
Optimization	5 [min]	29	144 [kB]

B. High-Altitude Flybys

The second example is a transfer problem from an Earth-bound orbit with $C \approx 3.6$ to a southern halo orbit with $C = 3.1$ associated with the L_1 libration point. High-altitude lunar flybys in resonance with the lunar orbital motion have been known to be useful in reducing fuel cost in such a transfer [22]. Recall that one of our aims is to demonstrate the versatility of the developed framework: it is applicable to the resonance-dominant region in a similar manner to the previous example of transfer between libration point orbits.

The detailed explanations of the processes that are identical to those in the previous example are omitted below. Table 3 summarize grid search conditions.

Table 3. Grid search conditions in the second example

Variable	Minimum	Maximum	Number of grids
x	-1	1	100
y	-1	1	
z	-0.75	0.75	
v_x^A	-2	2	
v_y^A	-2	2	
v_z^A	-2	2	
v_x^P	-10	10	
v_y^P	-10	10	
v_z^P	-10	10	

The initial conditions satisfying the following conditions are selected and propagated:

$R_e < r_1 < 1,\ r_2 > r_{Hill},\ C_{L3} < C < 4, i < 90$ [deg]
where R_e is the Earth's radius and i is the inclination with respect to the lunar orbital plane. Again, 121 graphs are generated from periapsis-to-periapsis arcs with $\Delta v_a^{max} = 200$ [m/s], $\Delta v_p^{max} = 0.5$, $\beta = 10$, and $\delta = 5$.

The initial arc is generated from perigee and apogee radii of 35000 [km] and 230000 [km], $i = 30$ [deg], and the argument of perigee with respect to the lunar orbital plane of 178 [deg] that are similar to the conditions at the first lunar flyby in SMART-1 [23]. The final arc (right panel) is a stable manifold emanating from an apogee state of the halo orbit with the perturbation magnitude of 10^{-4}.

As a result of pathfinding, 33 unique solutions are identified and those of the total transfer time shorter than 150 [days] are optimized. In the optimization process, perigee states are constrained to be higher than 20000 [km] from the surface of Earth.

Fig. 11 shows the optimized solutions. Distinct families are observed in an orderly manner in terms of the orbital resonance with the Moon indicating the applicability of the method to resonance-based transfer problems. The values of Δv are far from the theoretical minimum ($\approx$ 60 [m/s]) possibly due to the substantial inclination change.

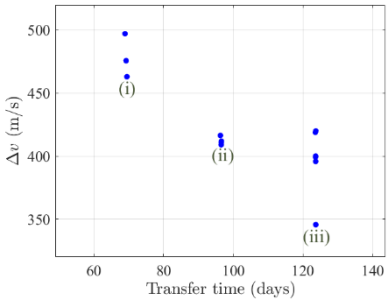

Fig. 11. Obtained solutions in the second example.

Figs. 12, 14, and 16 are initial guess trajectories of (i), (ii), and (iii) indicated in Fig. 11, respectively, and Figs. 13, 15, and 17 show the corresponding optimized solutions. The high-altitude lunar flybys reduce Δv required for changing orbital elements around Earth at the cost of long transfer time.

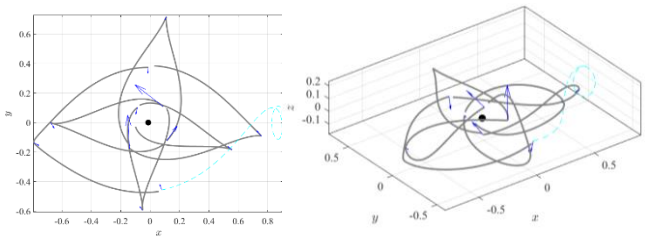

Fig. 12. Initial guess solution of (i). The dot, arrow, and dashed curve denote Earth, impulse, and stable manifold, respectively.

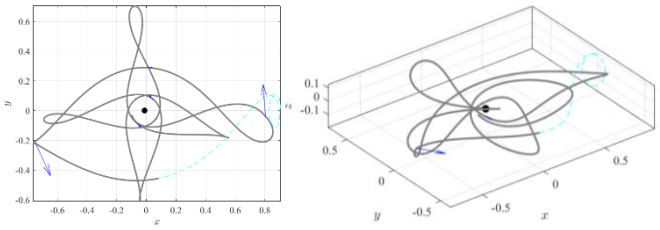

Fig. 13. Optimal solution (i). The dot, arrow, and dashed curve denote Earth, impulse, and stable manifold, respectively.

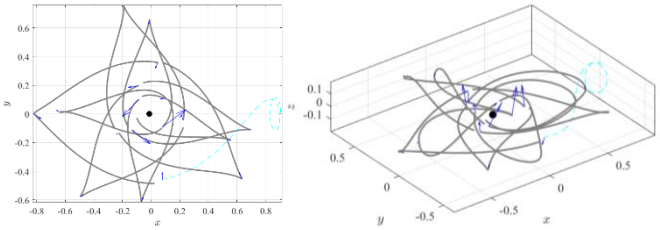

Fig. 14. Initial guess solution of (ii). The dot, arrow, and dashed curve denote Earth, impulse, and stable manifold, respectively.

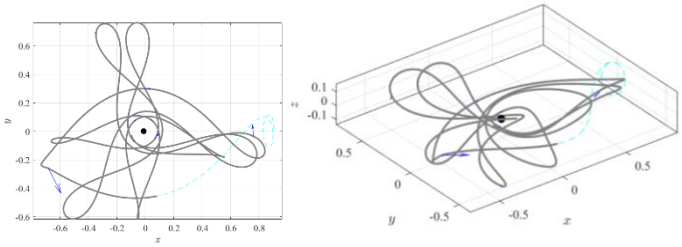

Fig. 15. Optimal solution (ii). The dot, arrow, and dashed curve denote Earth, impulse, and stable manifold, respectively.

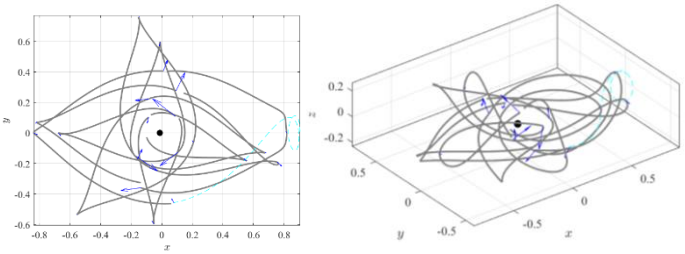

Fig. 16. Initial guess solution of (iii). The dot, arrow, and dashed curve denote Earth, impulse, and stable manifold, respectively.

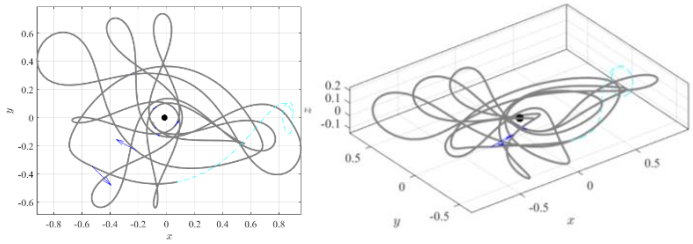

Fig. 17. Optimal solution (iii). The dot, arrow, and dashed curve denote Earth, impulse, and stable manifold, respectively.

Table 4 summarizes the computational performance. It is computationally lighter than the previous example indicating there is room for adopting finer grid search.

Again, the precomputing phase accounts for the majority of the running time.

Table 4. Computational performance in the second example

Process	Running time	Core	Output
Grid search	11 [min]	36	0.38 [GB]
Graph generation	3.7 [hour]	36	76.5 [GB]
Addition of boundary arcs and pathfinding	6 [min]	8	3 [kB]
Optimization	10 [min]	33	282 [kB]

V. ACKNOWLEDGEMENT

The author acknowledges the support from Society for Promotion of Space Science. This study has been partially supported by JSPS Grants-in-Aid No. 24K17448.

VI. REFERENCES

[1] K. Oguri, K. Oshima, S. Campagnola, K. Kakihara, N. Ozaki, N. Baresi, Y. Kawakatsu, and R. Funase, "EQUULEUS trajectory design," *J. Astronaut. Sci.*, vol. 67, pp. 950-976, 2020.

[2] G.A. Tsirogiannis, "A graph based methodology for mission design," *Celest. Mech. Dyn. Astr.*, vol. 114, pp. 353-363, 2012.

[3] E.W. Dijkstra, "A note on two problems in connexion with graphs," *Numer. Math.*, vol. 1, pp. 269-271, 1959.

[4] N.L. Parrish, "A* Pathfinding for Continuous-Thrust Trajectory optimization," *37th Annual AAS Guidance & Control Conference*, Breckenridge, January 2014.

[5] P.E. Hart, N.J. Nilsson, and B. Raphael, "A formal basis for the heuristic determination of minimum cost paths*," IEEE Trans. Syst. Sci. Cybern.*, vol. 4, pp. 100-107, 1968.

[6] A. Das-Stuart, K.C. Howell, and D.C. Folta, "Rapid trajectory design in complex environments enabled by reinforcement learning and graph search strategies," *Acta Astronaut.*, vol. 171, pp. 172-195, 2020.

[7] E. Trumbauer and B. Villac, "Heuristic search-based framework for onboard trajectory redesign," *J. Guid. Control Dyn.*, vol. 37, pp. 164-175, 2014.

[8] A. Bellome, J.P. Sánchez, L. Felicetti, and S. Kemble, "Multi-objective design of gravity assist trajectories via graph transcription and dynamic programming," *J. Spacecr. Rockets*, vol. 60, pp. 1381-1399, 2023.

[9] N. Hiraiwa, M. Bando, and S. Hokamoto, "Analysis of Transfer Trajectories in Cislunar Space Using Sequences of Lobe Dynamics," *74th International Astronautical Congress*, Baku, October 2023.

[10] W.S. Koon, M.W. Lo, J.E. Marsden, and S.D. Ross, "*Dynamical Systems, the Three-Body Problem and Space Mission Design*," Wellington: Marsden Books, 2011.

[11] R.H. Battin, "*An Introduction to the Mathematics and Methods of Astrodynamics*," New York: American Institute of Aeronautics and Astronautics, Inc., 1987.

[12] B.P. McCarthy and K.C. Howell, "Trajectory Design Using Quasi-Periodic Orbits in the Multi-Body Problem," *29th AAS/AIAA Space Flight Mechanics Meeting*, Ka'anapali, January 2019.

[13] K. Oshima, "Regularizing fuel-optimal multi-impulse trajectories," *Astrodyn.*, vol. 8, pp. 97-119, 2024.

[14] A. Celletti, "A. Basics of regularization theory," in *Chaotic Worlds: From Order to Disorder in Gravitational N-Body Dynamical Systems*. B.A. Steves, A.J. Maciejewski, and M. Hendry, Eds. Dordrecht: Springer, pp. 203-230, 2006.

[15] C.H. Yam, D. Izzo, and F. Biscani, "Towards a High Fidelity Direct Transcription Method for Optimisation of Low-Thrust Trajectories," *4th International Conference on Astrodynamics Tools and Techniques*, Madrid, May 2010.

[16] K.F. Sundman, "Memoire Sur le Probleme des Trois Corps," *Acta Math.*, vol. 36, pp. 105-179, 1912.

[17] K.E. Davis, "Locally optimal transfer trajectories between libration point orbits using invariant manifolds," *PhD Thesis*, University of Colorado Boulder, 2009.

[18] K.E. Davis, R.L. Anderson, D.J. Scheeres, and G.H. Born, "Optimal transfers between unstable periodic orbits using invariant manifolds," *Celest. Mech. Dyn. Astr.*, vol. 109, pp. 241-264, 2011.

[19] G.A. Tsirogiannis and V.V. Markellos, "A greedy global search algorithm for connecting unstable periodic orbits with low energy cost," *Celest. Mech. Dyn. Astr.*, vol. 117, pp. 201-213, 2013.

[20] G.A. Tsirogiannis and K.E. Davis, "A two-level perturbation method for connecting unstable periodic orbits with low fuel cost and short time of flight: application to a lunar observation mission," *Celest. Mech. Dyn. Astr.*, vol. 125, pp. 287-307, 2016.

[21] K. Davis, G. Born, and E. Butcher, "Transfers to Earth-Moon L_3 halo orbits," *Acta Astronaut.*, vol. 88, pp. 116-128, 2013.

[22] S. Campagnola, A. Boutonnet, J. Schoenmaekers, D.J. Grebow, A.E. Petropoulos, and R.P. Russell, "Tisserand-leveraging transfers," *J. Guid. Control Dyn.*, vol. 37, pp. 1202-1210, 2014.

[23] J. Schoenmaekers, "Post-Launch Optimisation of the SMART-1 Low-thrust Trajectory to the Moon," *18th International Symposium on Space Flight Dynamics*, Munich, October 2004.